Absolute Geodetic Rotation Measurement Using Atom Interferometry

J. K. Stockton, K. Takase, and M. A. Kasevich*

Department of Physics, Stanford University, Stanford, California 94305-4060, USA

(Received 27 March 2011; published 22 September 2011)

We demonstrate a cold-atom interferometer gyroscope which overcomes accuracy and dynamic range limitations of previous atom interferometer gyroscopes. We show how the instrument can be used for precise determination of latitude, azimuth (true north), and Earth's rotation rate. Spurious noise terms related to multiple-path interferences are suppressed by employing a novel time-skewed pulse sequence. Extended versions of this instrument appear capable of meeting the stringent requirements for inertial navigation, geodetic applications of Earth's rotation rate determination, and tests of general relativity.

DOI: 10.1103/PhysRevLett.107.133001 PACS numbers: 37.25.+k, 03.75.Dg, 06.30.Gv, 91.10.Pp

Atom interferometry has proven to be a solid technological foundation for inertial sensing [1]. In particular, atom interferometric gyroscopes [2–6] have reached performance levels where applications in fundamental tests of general relativity [7], Earth's rotation rate sensing for geodesy [8], and high accuracy inertial navigation [9] appear within reach.

In this Letter, we demonstrate a light-pulse atom interferometer gyroscope based on a pulse sequence which extends the dynamic range of previous sensors by a factor of 1000 and has an intrinsically calibrated rotation output. These attributes are enabling for the applications indicated above. Figure 1 shows the demonstrated configuration, in which momentum recoil from a pulse sequence of Doppler sensitive stimulated Raman transitions between ground state hyperfine levels coherently divides ($\pi/2$ pulse), redirects (π pulses), and recombines ($\pi/2$ pulse) atomic wave packets.

The phase sensitivity of the demonstrated $\pi/2$-π-π-$\pi/2$ interferometer pulse sequence (with temporal pulse spacings of T-$2T$-T) can be expressed as

$$\Delta\phi = 6\mathbf{k}_{\text{eff}} \cdot [(\mathbf{\Omega}_{\text{F}} + \mathbf{\Omega}_{\text{E}}) \times (\mathbf{g} + \mathbf{a})]T^3 - 2\mathbf{k}_{\text{eff}} \cdot (\mathbf{\Omega}_{\text{E}} \times \mathbf{g})T^3, \quad (1)$$

where $\mathbf{k}_{\text{eff}}$ is the effective propagation vector associated with the two-photon Raman transitions, the rotation vector of Earth is represented by $\mathbf{\Omega}_{\text{E}}$, and the rotation vector of the experimental apparatus with respect to the local, geostationary reference frame is represented by $\mathbf{\Omega}_{\text{F}}$. The acceleration of the apparatus with respect to this frame is parameterized by $\mathbf{a}$. This expression is derived in the short pulse limit and follows from straightforward application of the Feynman path-integral formalism as described, for example, in Refs. [10–12]. In our geometry, $\mathbf{k}_{\text{eff}}$ is approximately perpendicular to the local gravity vector $\mathbf{g}$. For clarity, we consider the limiting case of uniform angular velocity and accelerations.

When the sensor is geostationary, $\mathbf{\Omega}_{\text{F}}$ and $\mathbf{a}$ time average to zero, and the resulting shift is $\Delta\phi = 4\mathbf{k}_{\text{eff}} \cdot (\mathbf{\Omega}_{\text{E}} \times \mathbf{g})T^3$. The phase shift depends on the geodetic quantities $\mathbf{g}$ and $\mathbf{\Omega}_{\text{E}}$, while $\mathbf{k}_{\text{eff}}$ and T are known to high accuracy ($\mathbf{k}_{\text{eff}}$ is set by a laser locked to an atomic resonance and T by a high performance oscillator). Unlike conventional atom gyroscopes based on three-pulse sequences, this phase shift does not depend on atomic velocity. As a result, the interferometer is not subject to technical noise arising from drifts in this velocity or to contrast loss due to the velocity spread of the atomic source. The stability of the inferred rotation rate is instead limited by the value of $\mathbf{g}$ ($\mathbf{k}_{\text{eff}}$ and T are accurately known as described above). As we demonstrate below, interferometer contrast is observable at much larger rotation inputs than for a conventional three-pulse gyroscope.

A technical complication associated with this configuration is the fact that, as illustrated in Fig. 1, there exist spurious extra closed interference paths which arise from

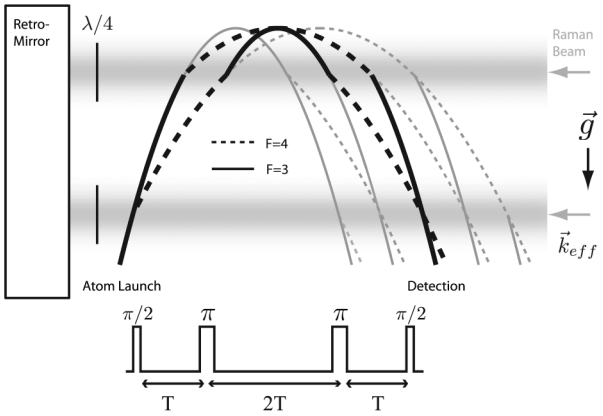

FIG. 1. The atom cloud is launched vertically with a slight horizontal velocity into the illustrated four-pulse Raman sequence. The retroreflected Raman beams are indicated by the two horizontal blurred lines, separated by a distance consistent with the pulse timing. The desired interferometer path is indicated with the black lines, and the undesired paths are indicated by the gray lines. The two closed three-pulse loops lead to spurious signals. A second atom fountain (to the right, similarly oriented and sharing the same optics) is not shown.

 © 2011 American Physical Society

imperfect Raman pulse areas. These paths add to and corrupt the main path signal. We demonstrate below that these interferences can be suppressed by adding a timing asymmetry, with the manageable trade-off of a slight acceleration sensitivity on the main path [12].

The experimental apparatus is depicted in Fig. 1 [13]. A vacuum cell containing two nearly identical cold Cs light-pulse interferometers is housed along with beam delivery optics and magnetic coils in a nearly cubic magnetic shield measuring less than $\lesssim 50$ cm per side. (The second Cs interferometer is used for diagnostic purposes, as described below.) All laser light is delivered to this unit with optical fibers. Within the vacuum cell, two-dimensional magneto-optic traps deliver transversely cooled Cs atoms to a pair of three-dimensional magneto-optic traps. Atoms are cooled, launched vertically with a slight horizontal velocity, and initialized within the $F = 3$, $m_F = 0$ state before encountering the horizontally oriented Raman beams which impart the necessary atom-optics pulses (both clouds interact with the same set of Raman beams). The Raman beams are frequency tuned to drive transitions between the $F = 3$, $m_F = 0$ and $F = 4$, $m_F = 0$ ground state hyperfine levels.

The Raman beams are derived from a single laser source imposed with sidebands via a fiber modulator, with the carrier and a first-order sideband providing the two photons necessary for the Raman transition. A retromirror scheme provides a common phase reference for the two-photon transition and allows observation of interference fringes despite the presence of phase fluctuations in the optics delivery path. With this scheme there are two possibilities for the directionality of the Doppler sensitive Raman transitions: the first photon being absorbed from the leftward beam and stimulated emission induced by the rightward beam or vice versa. The degeneracy between the two is lifted by the Doppler shift (approximately 100 kHz) from the nonzero mean velocity of the clouds along the propagation axes of the Raman beams. This shift is set to be greater than that from the thermal spread so that the excitation directionality can be selected by adjusting the sideband detuning. The Raman beams were made as large and uniform as possible to enhance interferometer contrast, with semiconductor laser tapered amplifiers supplying the needed optical power to enable Raman π pulses approximately 18 μs in duration [14]. The Raman pulses were aligned to allow for the four-pulse gyroscope sequence ($\pi/2$-π-π-$\pi/2$) with pulse spacing of T-$2T$-T with $T = 51.5$ ms.

After the final Raman pulse, the atoms are detected with the scheme discussed in Ref. [15], which mitigates the effects of atom number fluctuations by detecting both atomic ground states to perform normalized detection. Furthermore, the detectors were apertured to a smaller size such that only the cold central portion of each atom cloud was detected. Although this caused a decrease in signal, for our operating conditions it enhanced the contrast and signal-to-noise ratio. As a result, the detection samples a small subset of the total atom number (approximately 10^5) at a sub-μK effective temperature.

As mentioned above, there exist multiple interference paths in a four-pulse interferometer due to imperfect Raman pulses. However, the undesired paths can be made incoherent by providing a timing skew dT in the pulse sequence of the form $(T - dT) - 2T - (T + dT)$, so that they do not lead to closed interferometers. This occurs when the path imbalance $\delta x \sim v_{\mathrm{rec}} dT$ (v_{rec} is the Raman transition recoil velocity) is much greater than the thermal de Broglie wavelength of the atom source (~ 10 nm in this work). For a geostationary sensor, this timing asymmetry introduces an acceleration sensitivity in the remaining closed interferometers of the form

$$\Delta\phi_g = 4\mathbf{k}_{\mathrm{eff}} \cdot \mathbf{g} T dT = 4|\mathbf{k}_{\mathrm{eff}}||\mathbf{g}| \sin(\theta_{\mathrm{tilt}}) T dT. \quad (2)$$

In our experiment this term most readily contributes at low frequencies through the tilt θ_{tilt} of the sensor, which produces a sensitivity of 300 mrad of phase per milliradian of tilt for $dT = 100$ μs. We exploit this tilt sensitivity to measure and zero the tilt of the sensor (in order to establish the orthogonality of $\mathbf{k}_{\mathrm{eff}}$ and $\mathbf{g}$). We subsequently suppress this sensitivity through shot-to-shot reversal of the sign of dT. This has the effect of periodically reversing the sign of this contribution to the total phase shift, so that the sum of two successive measurements is insensitive to residual tilt drifts.

The elimination of the multiple-path terms is demonstrated in Fig. 2. For these data, we parametrically plot the normalized interferometer transition probabilities of the two nearly identical interferometers. These interferometers are spatially displaced by 20 cm along the horizontal axis but otherwise share the same set of Raman beams. Because of unavoidable asymmetries between the interferometers, the Raman excitation efficiencies are not perfectly balanced. Without multiple-path contributions ($dT = 100$ μs), the result is a relatively smooth ellipse (shown in black) due to the presence of only one closed interferometer in each output. However, when the multiple-path contributions are present ($dT = 0$ μs), the result is blurred (shown in gray). The overall relative phase of the two interferometer outputs is tuned with a short magnetic field pulse inserted between the first and second Raman pulses.

We confirmed the predicted sensitivity of the gyroscope to Earth's rotation [Eq. (1)] by mounting the sensor on a horizontally oriented turntable and measuring the Earth-rotation-induced phase shift at a series of discrete, stationary turntable orientations. The sensor was operated in propagation vector-reversal mode, where, on successive measurement trials, the signs of $\mathbf{k}_{\mathrm{eff}}$ and dT are reversed [5]. In addition to suppressing tilt terms, this method cancels sources of technical noise that do not change sign with the reversal, such as spurious phase shifts from magnetic fields and residual ac Stark shifts associated with

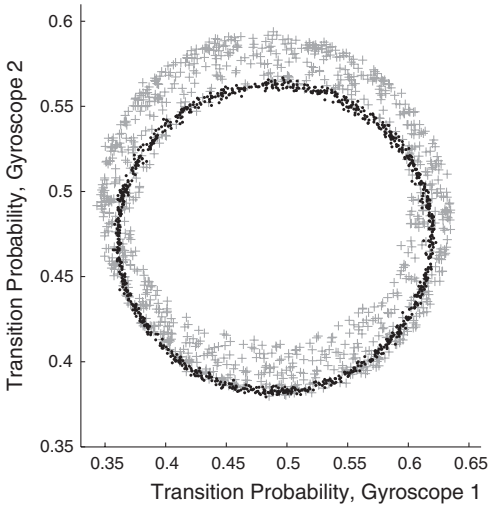

FIG. 2. Experimental demonstration of multiple-path elimination. The transition probabilities from the two gyroscope outputs are plotted parametrically for $dT = 100$ μs (black, multipath eliminated) and $dT = 0$ μs (gray, multipath present). The transition probabilities are obtained from measurements of the number of atoms in each of the two hyperfine levels following the interferometer pulse sequence. The two interferometer outputs were tuned to be $\pi/2$ radians out of phase.

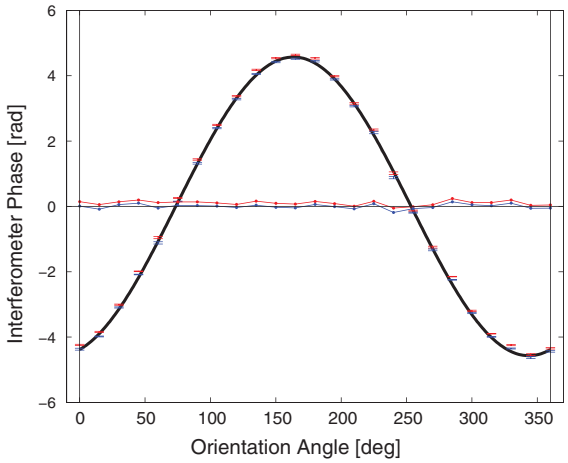

FIG. 3 (color). Measurement of Earth's rotation rate as a function of sensor orientation angle in lab coordinates. Solid points indicate outputs of the two interferometers (red and blue). The black sinusoid is a fit to the data. Also shown are the fit residuals. The phases were determined from fitting sinusoids to the interferometer outputs. The interferometer fringes were scanned by electro-optically adjusting the phase of the final Raman pulse.

the Raman excitation. The sinusoidal modulation in the observed phase shift reflects the change in the relative angle between $\mathbf{k}_{\text{eff}}$ and $\mathbf{g} \times \mathbf{\Omega}_{\mathbf{E}}$ as $\mathbf{k}_{\text{eff}}$ is rotated. The measured signal is shown in Fig. 3, and the amplitude of the response agrees to within 0.05% of the expected shift, given independent knowledge of latitude, local gravity, and Earth's rotation rate. This result is obtained without any fit or calibration parameters. The tilt sensitivity described above was used to establish the orthogonality between $\mathbf{k}_{\text{eff}}$ and $\mathbf{g}$ to better than 1 mrad. This plot also demonstrates the potential utility of this apparatus for azimuth determination applications, where the sinusoid midpoints indicate true north.

We characterized the sensitivity of the gyroscope under external rotations of the sensor ($\mathbf{\Omega}_F$ above) by actively rotating the apparatus about the axis mutually perpendicular to $\mathbf{k}_{\text{eff}}$ and $\mathbf{g}$. For these measurements, shown in Fig. 4(a), the rotational motion was actuated with sinusoidally driven (0.7 Hz frequency) piezoelectric stacks. The induced motion was characterized by the observed deflection of a laser beam, whose source was anchored to the apparatus on a quadrant photodetector located a distance of 3 m from the sensor. The induced rotation rate was independently confirmed with a calibrated tilt sensor (Applied Geomechanics, 755-1129). Interferometer data were acquired when the relatively short (200 ms) interferometer sequence occurred on the linear slope of the sinusoidal rotation modulation. The results are shown in Fig. 4(a), where the measured phase shift prefactor [Eq. (1)] is consistent with the expected result of six, as opposed to the factor of 4 for Earth's rotations.

We showed that interferometer contrast can be achieved at large rotation rates [Fig. 4(b)]. For these measurements, we actuated relatively large uniform rotational motion about the vertical axis by using a precision turntable (Contraves Goerz Corporation, Servo Controller 403, Direct Drive Precision Rate Table 722). We inferred the interferometer contrast from the amplitude parametric response curves (shown in Fig. 2) as a function of the table rotation rate. We observed that contrast could be maintained for rotation rates in excess of 0.1 rad/s. This observed dynamic range is more than 3 orders of magnitude larger than the dynamic range demonstrated with previous atom interferometer sensors [3,16] based on the $\pi/2$-π-$\pi/2$ excitation sequence. For these earlier sensors, the velocity spread of the laser-cooled atomic source, coupled with the Coriolis phase shift $2\mathbf{k}_{\text{eff}} \cdot (\mathbf{v} \times \mathbf{\Omega})T^2$, leads to contrast loss at relatively modest rotation rates. For example, for a velocity spread of $\delta v \sim 1$ cm/s (μK temperatures) and $T = 100$ ms, a rotation rate of as little as 0.7 mrad/s will lead to $\delta\phi \sim 1$ rad and hence a significant loss of contrast. In our case, the timing offset dT introduces a residual Coriolis acceleration sensitivity, as described above, that ultimately limits contrast.

Finally, we characterized sensor noise, distinguishing inertial noise (caused by motion on the time scale of T) from the noise floor of the sensor (determined by detection noise, e.g., atom shot noise). In Fig. 5(a), we plot the output of each interferometer under typical conditions. To infer the true noise (without inertial motion, as would be measured at a quiet facility), we align the fringes (with a magnetic field pulse) to sit on the side of each fringe and determine the differential phase ϕ_D by subtracting the two

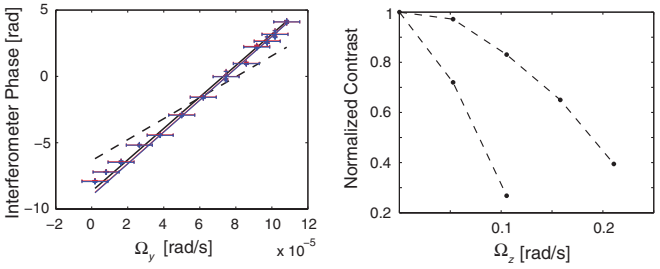

FIG. 4 (color). (a) Phase shift as a function of induced rotation about the axis mutually perpendicular to $\mathbf{k}_{\mathrm{eff}}$ and $\mathbf{g}$. Red and blue points indicate outputs of each of the two interferometers, respectively. The solid black line is a fit to the data by assuming a fixed prefactor of six and adjusting only the offset, while the dashed black line assumes a fixed prefactor of four. A fit to the data at higher rotation rates gives an estimated slope of 6.07 ± 0.2. (b) Normalized contrast as a function of rotation rate about the vertical axis. Contrast was determined by fitting 100-point parametric ellipses. The upper curve is for a $dT = 20$ μs, and the lower curve is for a larger time asymmetry $dT = 500$ μs, demonstrating that the performance is limited in part by the acceleration sensitive term.

interferometer phases. The noise of ϕ_D provides an upper limit of the noise floor for each individual sensor without inertial noise. The noise on the differential phase is 14.4 mrad, which, along with a repetition rate of $\tau = 0.5$ s, gives an implied angle random walk of 8.5×10^{-8} rad/s/Hz$^{1/2}$ ($295\ \mu$ deg $/\sqrt{\mathrm{hr}}$) using Eq. (1). The differential angle random walk is consistent with estimates of atomic shot noise to within a factor of order unity. For comparison, the inertially induced noise for a single interferometer is ~540 mrad, limited by spurious rotations of the test platform.

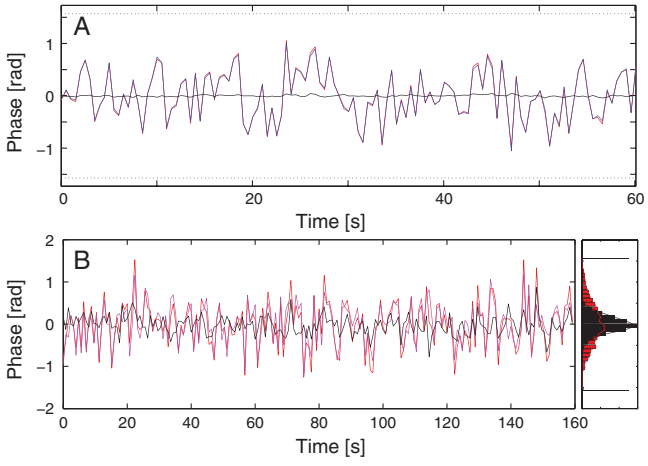

FIG. 5 (color). (a) Output of parallel interferometers (red and blue) and the subtracted signal (black). (b) Output of a single sensor sitting on the side of the fringe (red), predicted signal from the auxiliary sensor (purple), derived from the measured rotation rates during the pulse sequence, and the subtracted residual (black). Corresponding histograms indicating 60.5% cancellation, limited by the auxiliary sensor noise floor.

In many practical applications, high-frequency inertial noise will be present. Here we demonstrate the use of auxiliary sensors to manage this noise, thus enabling high accuracy rotation measurements in inertially noisy environments. We attached an angle rate sensor (ATA ARS-12) to the apparatus and processed its record to predict the high-frequency angle jitter of the retromirror at each interferometer pulse. We used this information to predict the phase shift of the atom interferometer due to high-frequency fluctuations. We correlated the predicted phase shift with the atom interferometer output when the interferometer was biased to operate on the side of an interference fringe. The results are shown in Fig. 5(b). Although this cancellation is done in postprocessing, there also exists the possibility of actively compensating these fluctuations in real time. The development of a similar scheme using accelerometers in feed-forward mode is discussed in Ref. [17].

It is interesting to consider possible future applications of this sensor configuration. For example, a terrestrial apparatus with $T = 700$ ms, operating at a 2000:1 signal-to-noise level per shot, would achieve a sensitivity of 2×10^{-12} rad/s per shot or roughly 30 ppb of Earth's rotation rate per shot (roughly the size of the geodetic precession term of general relativity [18]). Such a configuration could be realized in the 10 m atomic fountain currently under development at Stanford. On the other hand, a satellite sensor would be able to maintain contrast at the high rotation biases associated with satellite orbits [19]. Finally, a compact, optimized sensor could be used for high accuracy inertial navigation applications [9].

We thank Boris Dubetsky for helpful conversations, Todd Gustavson for guidance in design and fabrication of the sensor, and AOSense, Inc. for assistance in fabrication of the sensor. This work was supported by Navy DMP06035 and DARPA W911NF-06-1-0064.

*kasevich@stanford.edu

[1] *Atom Interferometry*, edited by P. R. Berman (Academic, San Diego, 1997).
[2] T. L. Gustavson, P. Bouyer, and M. A. Kasevich, Phys. Rev. Lett. **78**, 2046 (1997).
[3] T. L. Gustavson, A. Landragin, and M. A. Kasevich, Classical Quantum Gravity **17**, 2385 (2000).
[4] A. Lenef, T. D. Hammond, E. T. Smith, M. S. Chapman, R. A. Rubenstein, and D. E. Pritchard, Phys. Rev. Lett. **78**, 760 (1997).
[5] D. S. Durfee, Y. K. Shaham, and M. A. Kasevich, Phys. Rev. Lett. **97**, 240801 (2006).
[6] B. Canuel *et al.*, Phys. Rev. Lett. **97**, 010402 (2006).
[7] S. Dimopoulos, P. W. Graham, J. M. Hogan, and M. A. Kasevich, Phys. Rev. D **78**, 042003 (2008).
[8] W. H. K. Lee, M. Celebi, M. I. Todorovska, and H. Igel, Bull. Seismol. Soc. Am. **99**, 945 (2009).

[9] A. Chatfield, *Fundamentals of High Accuracy Inertial Navigation* (AIAA, Reston, 1997).
[10] P. Storey and C. Cohen-Tannoudji, J. Phys. II (France) **4**, 1999 (1994).
[11] K. Bongs, R. Launay, and M. Kasevich, Appl. Phys. B **84**, 599 (2006).
[12] B. Dubetsky and M. Kasevich, Phys. Rev. A **74**, 023615 (2006).
[13] See also K. Takase, Ph.D. thesis, Stanford University, Stanford, CA, 2008.
[14] K. Takase, J. K. Stockton, and M. A. Kasevich, Opt. Lett. **32**, 2617 (2007).
[15] G. W. Biedermann, X. Wu, L. Deslauriers, K. Takase, and M. A. Kasevich, Opt. Lett. **34**, 347 (2009).
[16] J. McGuirk, G. Foster, J. Fixler, M. Snadden, and M. Kasevich, Phys. Rev. A **65**, 033608 (2002).
[17] F. Yver-Leduc, P. Cheinet, J. Fils, A. Clairon, N. Dimarcq, D. Holleville, P. Bouyer, and A. Landragin, J. Opt. B **5**, S136 (2003).
[18] N. Strauman, *General Relativity with Applications to Astrophysics* (Springer, New York, 2006).
[19] *Space Mission Analysis and Design*, edited by J. Wertz and W. Larson (Springer, New York, 1999).